Contents lists available at ScienceDirect

Chemical Engineering Research and Design

journal homepage: www.elsevier.com/locate/cherd

Multiscale computational fluid dynamics modeling of thermal atomic layer deposition with application to chamber design

Yichi Zhang [a], Yangyao Ding [a], Panagiotis D. Christofides [a,b,*]

[a] Department of Chemical and Biomolecular Engineering, University of California, Los Angeles, CA 90095-1592, USA
[b] Department of Electrical and Computer Engineering, University of California, Los Angeles, CA 90095-1592, USA

ARTICLE INFO

Article history:
Received 1 May 2019
Received in revised form 15 May 2019
Accepted 17 May 2019
Available online 25 May 2019

Keywords:
Atomic layer deposition
Microscopic modeling
Computational fluid dynamics modeling
Kinetic Monte Carlo modeling
Geometry optimization
ALD cycle time optimization

ABSTRACT

This work develops a first-principles-based three-dimensional, multiscale computational fluid dynamics (CFD) model, together with reactor geometry optimizations, of SiO_2 thin-film thermal atomic layer deposition (ALD) using bis(tertiary-butylamino)silane (BTBAS) and ozone as precursors. Specifically, an accurate macroscopic CFD model of the ALD reactor chamber gas-phase development is integrated with a detailed microscopic kinetic Monte Carlo (kMC) model that was developed in Ding et al. (2019), accounting for the microscopic lattice structure, atomic interactions and detailed surface chemical reactions. The multi-scale information exchange and the transient simulation of the microscopic distributed kMC algorithms and the macroscopic CFD model are achieved through a parallel processing message passing interface (MPI) structure. Additionally, density functional theory (DFT)-based calculations are adopted to compute the key thermodynamic and kinetic parameters for the microscopic thin-film growth process. Recognizing the transient non-uniformity and the possibility to reduce the current ALD cycle time, the optimal configuration of reactor geometry is designed and evaluated including a showerhead panel adjustment and geometry modifications on reactor inlet and upstream. It is demonstrated that with suitable reactor chamber design the required BTBAS ALD half-cycle time can be reduced by 39.6%.

1. Introduction

Thin-film deposition has always been an important upstream component of the semiconductor industry. To produce good-quality thin-films, many deposition techniques, such as physical vapor deposition (PVD), coating, and chemical vapor deposition (CVD) have been developed over the past few decades for materials like amorphous silicon, Al_2O_3, ZrO_2, HfO_2 and other (Nalwa, 2002). Nevertheless, more precise and controllable deposition technology is needed as the requirements in semiconductor industry have become increasingly stringent. For example, the new memory designs like the NAND-type flash memory require conformal films with a more stringent criterion on uniformity and defects, along with complex non-planar three-dimensional structures. In addition, the dimensions of the new gate dielectrics are scaling down to sub-10-nm scale, with the associated film thickness under 20 Å (George et al., 1996; Schuegraf et al., 2013). To meet the demands of such major design breakthroughs, atomic layer deposition (ALD) process has been developed and widely utilized in the semiconductor industry (Kääriäinen et al., 2013). ALD is a thin-film deposition method originally developed as a subclass variation of CVD. In ALD processes, the substrate surface is sequentially exposed to gas-phase precursor pulses

* *Corresponding author at*: Department of Chemical and Biomolecular Engineering, University of California, Los Angeles, CA 90095-1592, USA.
E-mail address: pdc@seas.ucla.edu (P.D. Christofides).
https://doi.org/10.1016/j.cherd.2019.05.049

instead of a single continuous flow of gas stream. In each of these pulses (half-cycle), ideally only precursor is reacting with the surface in a self-limiting way, which allows a nearly conformal surface coverage under sufficient cycle time, precursor dosage and appropriate operating conditions. Between the alternating half-cycles, an inert gas is used to purge the reactor, removing the previously-entered precursor from the chamber prior to the next precursor pulse, in order to avoid undesirable reactions and to ensure high film quality (George, 2009). Thus, the ALD method is capable of uniformly growing materials layer-by-layer on complex substrate geometries in a more precise and more controllable manner (Tanner et al., 2007; Foong et al., 2010; Shirazi and Elliott, 2014; Ishikawa et al., 2017). As a result, ALD has demonstrated its great potential in the field of microelectronics manufacturing, where 3D ultra-thin and highly-conformal films are becoming increasingly crucial.

In recent years, there has been a growing number of ALD works on both laboratory and industrial scales for developing novel reaction mechanisms and precursors, which allow higher aspect ratio substrate lay-outs and faster film processing (Kääriäinen et al., 2013). Nevertheless, industrial manufacturing and experimental studies on ALD still struggle with limited throughput and high cost of precursors and ALD equipment (Shirazi and Elliott, 2014). In addition, the exact influence of the gas-phase development in the reactor on the microscopic deposition processes remains unclear, and the real-time in-situ monitoring of film growth uniformity and local structure is not yet industrially available. Detailed molecular structure can be investigated using scanning electron microscope (SEM) and scanning tunneling microscope (STM), which are destructive to the deposited film (Schwille et al., 2017b). Real-time overall thin-film growth rate may be examined with quartz crystal microbalance (QCM) but the measurement of local deposition rates is beyond QCM's capability (Elam et al., 2002). In-situ spectroscopic ellipsometry is a feasible method for local behavior inspection but currently it is not prevalent in the industry because of its complex optical operations (Pittal et al., 1993; Dalton et al., 1994). Thus, a comprehensive simulation model for ALD reactor chambers that helps understanding the details of the real-time reactor gas-phase profile together with the thin-film deposition profile is of value to both industrial and research work.

Many simulation models have been developed to capture the transport phenomena in the gas-phase for CVD, as well as the reaction and structural details of the thin-film deposition. For the gas-phase model, traditionally, analytical solutions of the mass, momentum and energy conservation equations are obtained to characterize the macroscopic gas-phase spatio-temporal evolution in simplified geometries and with very low computational demand. For example, Christofides et al. (2008) assumed a 2D vertical flow gas-phase profile, and Schwille et al. (2017a) constructed the reactor chamber geometry with a simple array of equally sized square-shaped cells. However, the first-principles models with simplified assumptions fail to provide meaningful results that are applicable to the industrially-relevant ALD systems, which often involve complicated and detailed reactor geometry designs. Thus, computational fluid dynamics (CFD) modeling, a more advanced numerical simulation tool, is adopted and it is demonstrated to be capable of solving the gas-phase transport phenomena with high resolution in complex geometries (Pan et al., 2014; Crose et al., 2018). For the microscopic surface deposition model simulation, Molecular Dynamics (MD), and more recently, kinetic Monte Carlo (kMC) are broadly utilized (Elliott and Greer, 2004; Crose et al., 2015; Weckman et al., 2018). Ab initio MD models monitor the physical movement of all atoms and molecules in the system, which is computationally impossible and ill-conditioned for the industrial-scale systems (Battaile and Srolovitz, 2002). On the contrary, the kMC method tracks a single event according to its probability distribution at a given time, dramatically improving the computational efficiency while preserving the model validity (Rey et al., 1991; Dkhissi et al., 2008). Many groups have demonstrated the possibility of incorporating kMC in ALD simulations. For example, Knoops et al. (2010) adopted the experimentally determined reaction and recombination probabilities to construct a simple kMC algorithm for plasma-enhanced ALD. Shirazi and Elliott (2014) simulated Al_2O_3 ALD on small-scale using a first-principles analysis based kMC model. Recently, Crose et al. (2018) proposed a multiscale CFD modeling approach, integrating the microscopic kMC model and a macroscopic CFD model for plasma enhanced CVD, and demonstrated its ability to help understanding the influence of the reactor geometry on the microscopic surface deposition profile.

In semiconductor manufacturing, SiO_2 is one of the most crucial materials for the sacrificial layers in micro-electro-mechanical systems (MEMS) and dielectric films for metal-oxide-semiconductor field-effect transistor (MOSFET) (Bühler et al., 1997; Murray et al., 2014). The film thickness of those ultra-thin gate oxides has decreased to around 20 Å (10 atomic layers) and it is not possible to produce such thin films using traditional deposition methods (Schuegraf et al., 2013). Recently, Ding et al. (2019) has investigated the detailed mechanism of the microscopic SiO_2 thin-film deposition using thermal ALD. However, that work has not incorporated the microscopic deposition profile with the gas-phase development in the thermal ALD reactor. In order to fully understand the entire SiO_2 ALD process, it is essential to adopt the multi-scale approach developed by Crose et al. (2018). The resulting transient multiscale CFD model will provide a full-picture of the deposition process and enable a better understanding of the input–output relationship between operation conditions and cycle time. Having an accurate and comprehensive model also makes on-line optimization and real-time control possible for ALD processes (Wang et al., 2009; Kwon et al., 2015a,b; Rasoulian and Ricardez-Sandoval, 2015, 2016; Oh and Lee, 2016; Chaffart and Ricardez-Sandoval, 2017, 2018).

In this paper, we propose a density functional theory (DFT)-based multiscale CFD model for SiO_2 thin-film ALD with bis(tertiary-butylamino)silane (BTBAS) and ozone as precursors. Specifically, the multiscale CFD model combines a 3D macroscopic CFD domain and a 3D microscopic surface deposition kMC domain. The DFT-calculated thermodynamic and kinetic parameters such as the intermediate complex activation energies and the pre-exponential coefficients crucially affect the event selection of the microscopic kMC model to reproduce realistic thin-film growth rates and structure. Additionally, entropy, enthalpy, and viscosity are critical to the gas-phase CFD transport phenomena. With regard to the microscopic domain (i.e., the surface of the SiO_2 wafer), a detailed 3D kMC algorithm developed previously by Ding et al. (2019) is adopted to capture the structure of the SiO_2 thin-film, the reaction mechanism, and the growth profile. For the macroscopic domain (i.e., the gas-phase), a transient 3D CFD model is adopted to account for the coupled mass and energy transport in the industrial scale ALD reac-

tor under experimental and industrial standard operating conditions. The macroscopic and microscopic domains are linked and solved simultaneously via a parallel processing message passing interface (MPI) structure. A nominal reactor design under the proposed model successfully reproduces the experimental and industrial growth per cycle (GPC) and cycle time, and the result reveals a non-uniform transient development of the precursor concentration in the reactor. According to this finding, two chamber geometry designs are developed and evaluated, including an adaptive adjustment of the size and position of showerhead holes, and a modification of the upstream region (Lee et al., 2006). The resulting optimal chamber design adjusts and integrates the two features and is demonstrated to reduce the half-cycle time needed by 39.6%. Furthermore, the integrated modeling framework developed in this work can serve as a general modeling guideline for ALD and can be extended to other thin-film materials using different precursors, reactors, and operating conditions.

2. ALD process description and multiscale CFD modeling

This section focuses on the development of the 3D multiscale CFD model that describes the thermal ALD deposition of SiO_2 thin-film, which is demonstrated in Fig. 1. The precursor selection is first discussed based on the candidates' reported chemical and physical properties. Then, the CFD model for the gas-phase macroscopic domain is discussed in detail: a 3D geometry of a thermal ALD reactor is constructed and is discretized spatially to a high-quality mesh; the gas-phase transport mechanisms and the detailed tuning are elaborated. Next, the kMC algorithm for the microscopic deposition model is discussed in detail: the approximation of the 3D SiO_2 lattice is introduced and validated; the reaction mechanism and associated kinetics are formulated; the kMC algorithm for event selection and time evolution is explained. Subsequently, the parallel processing and the interaction between the two models through the MPI is demonstrated along with the automated workflow. Finally, DFT calculations using Gaussian09/Gaussview software package for the determination of the important thermodynamic parameters are explained (Frisch et al., 2000).

2.1. Precursor selection

The choice of the Si precursors in the SiO_2 ALD process is one of the most important factors that determines the growth rate and the quality of SiO_2 thin-films. In recent studies, aminosilane-based precursors have gained significant popularity because the H-N hydrogen bonds formed between the precursor particles and the substrate surface significantly lower the reaction energy barrier and hence improve SiO_2 deposition (O'Neill et al., 2011). As demonstrated in Ding et al. (2019), we choose BTBAS as the Si half-cycle precursor because of its fast growth rate (1.4 Å ~ 2.1 Å per cycle), sufficient experimental and industrial data, and detailed theoretical reaction mechanisms (O'Neill et al., 2011; Han et al., 2011). For the oxygen precursor, we choose ozone (O_3) among the common candidates for thermal ALD of oxide films, which is extensively studied in the laboratory and utilized in the industry (Nishiguchi et al., 2002; Prechtl et al., 2003; Han et al., 2011).

2.2. Macroscopic CFD model

Deposition of SiO_2 thin-films in an industrial ALD reactor is intimately related to the physical and chemical phenomena that govern the gas-phase. In order to obtain an accurate characterization of velocity, concentration and temperature profile, the coupled continuity, energy, and mass balance equations need to be solved in 3D domain defined by the proposed reactor geometry. Computational fluid dynamics is specifically tailored to tackle such tasks. In this work, we utilize ANSYS Fluent 19.2 software package, a commercial CFD simulation software, to construct the reactor geometry, perform meshing and solve for the gas-phase profile (Fluent, 2013).

2.2.1. Reactor design and meshing

Various thermal ALD reactor geometries are used in industry. In our model, we adopt a cylindrical showerhead reactor chamber based on the design of EmerALD XP by ASM International (Lee et al., 2006). Specifically, the reactor chamber is scaled to accommodate for processing the up-to-date industrial 300 mm wafer, with the exact dimension shown in Fig. 2(a) (King, 2011). Precursor gas is introduced from the top of the reactor, labeled 1, and develops uniformly in the upstream region, labeled 2. Then, precursor gas flows through the showerhead holes, labeled 3, falls onto the substrate surface, labeled 4, and then exits through the bottom outlet that is connected to a vacuum pump, labeled 5. The nominal showerhead design contains 10 mm-diameter showerhead holes, uniformly spaced in a rectangular array across the showerhead region, while the optimized designs of showerhead and upstream regions will be discussed in Section 3. The 3D ALD reactor geometry is constructed in AUTOCAD, a 3D computer-aided design software. It is important to capture the 3D detail because the showerehad design is complicated and not azimuthally symmetric for a 2D axisymmetric characterization. Next, the resulting geometry is exported to the ANSYS Design Modeler for spatial discretization, which is necessary for the hybrid meshing mentioned below. The discretized components are then recombined to a single fluid body after sectioning in order to ensure zone conformity (Fluent, 2013).

In CFD, the governing transport PDEs need to be solved in smaller subdomains made of geometric primitives, split from the major geometry. The collection of those geometry primitives is called a mesh. Because the governing equations will be discretized and solved inside each of these subdomains using the finite volume method, the meshing resolution and quality are crucial for the overall CFD accuracy (Eymard et al., 2000). Two meshing strategies are generally adopted: structured mesh and unstructured mesh. While unstructured mesh is a more straight-forward approach and is faster in implementation, it leads to longer simulation computation time due to the geometric irregularity and the large number of cells in the resulting mesh. On the contrary, performing a fully structured meshing on our reactor geometry may improve the computational efficiency but is labor and time-consuming. Any adaptive structural optimization of the reactor design will require a complete manual re-mesh. Therefore, in this work, a hybrid mesh is chosen as a balance between the two approaches. Using ANSYS Meshing, we adopt a multizone method to discretize the single body. Structured mesh with hexahedral elements is used for the majority of reactor geometry that has simpler overall geometry. By contrast, unstructured meshing is performed on the showerhead and

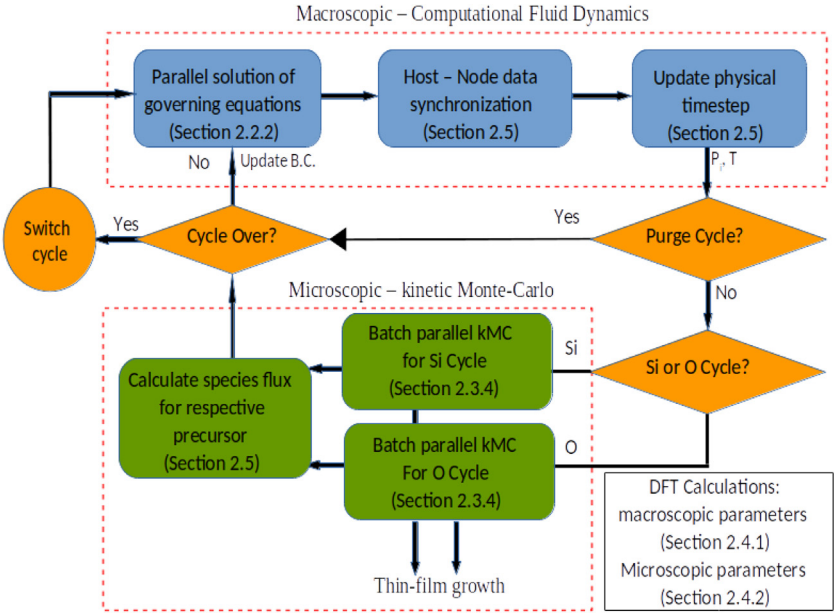

Fig. 1 – Multiscale workflow, parallel processing and information exchange illustration. (For interpretation of the references to color in the text, the reader is referred to the web version of this article).

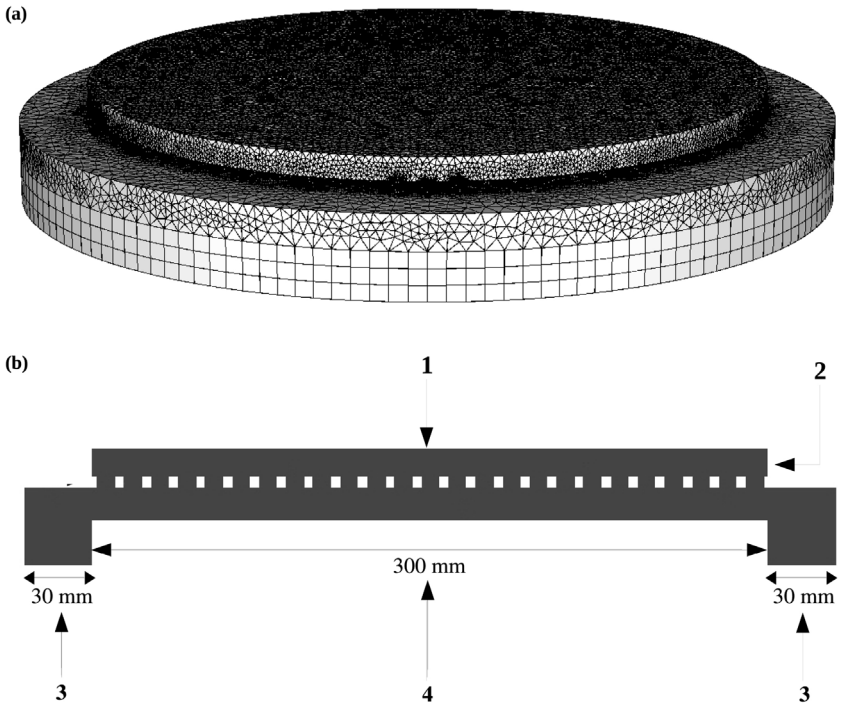

Fig. 2 – Mesh and *x*-cross-section geometry of the nominal reactor.

substrate surface regions, which have high aspect ratio and more predefined geometric irregularities. Patch independent tetrahedral meshing method with high relevance is adopted to discretize such areas with good precision to obtain good cell quality for computational accuracy and efficiency.

Mesh independence test is carried out, where the smallest mesh produced for an invariant simulation result is chosen so that the best computational efficiency can be achieved without influencing the simulation accuracy. Meshes containing 2 to 2.5 million cells are proved to produce mesh independent results depending on the specific reactor geometries. The resulting mesh is demonstrated to have a good quality, which is characterized by the overall quality, skewness and aspect ratio. Table 1 shows the acceptable range of each parameter with * being the desired value, and the corresponding quality of our meshes from the nominal design to the final optimized design, respectively. The data shows that the min/max bounds of each mesh quality metric lie within the acceptable range and the average mesh metrics lie close to the ideal values. The three factors and their recommended value ranges are

Table 1 – Cell quality of the nominal and final design hybrid reactor mesh, with * being the desired value of each metric.

	Acceptable range	Nominal bound; average	Final bound; average
Quality	0–1*	0.34; 0.79	0.33; 0.79
Skewness	0*–0.95	0.69; 0.29	0.74; 0.29
Aspect ratio	1*–100	5.41; 1.99	6.49; 1.98

suggested by the manufacturer ANSYS Inc. (Fluent, 2013; Tran et al., 2017). Other optimized designs have shown similar quality.

2.2.2. Gas-phase transport model

In the macroscopic domain, a transient model is applied in CFD using ANSYS Fluent pressure-based solver. The built-in transport models and several user defined functions (UDFs) are implemented to apply ALD process specifications on the materials, transport phenomena, as well as operating and boundary conditions.

Three gas species are used in the Fluent simulation. Argon is the purging gas in between Si-Cycle and O-cycle. BTBAS and ozone are the Si-cycle and O-cycle precursors, respectively, which are involved in the surface reactions that will be introduced in more detail in Section 2.3.2. The other reaction by-products are proved not important in the convention-dominated gas-phase profile, and thus, it is not included in the CFD. Argon, ozone are selected from the Fluent Database, while BTBAS is defined with DFT-calculated and literature values: the molecular weight equals to 174.36 g/mol; viscosity is approximated with a linear fit of 5.582×10^{-6} kg/m-s at 398 K and 6.824×10^{-6} kg/m-s at 600 K (Bird et al., 2007); the specific heat (C_p) is characterized as a piecewise-polynomial fit with coefficients $A = -4.1113$, $B = 1.0243$, $C = -0.0005$ under Fluent input format (Fluent, 2013); standard enthalpy is determined to be −267.84 kcal/mol, and the standard entropy is determined to be 126.79 cal/mol-K. Viscosity, enthalpy, entropy and C_p are calculated using DFT and thermodynamic principles, which will be discussed in Section 2.4. The mixture of gas species is defined using the Fluent Mixture Template (Fluent, 2013). The mixture is assumed to be an incompressible ideal gas mixture, appropriate for a laminar system with Mach number smaller than 0.3, which is valid for all inlet flow rates and operating pressures considered in this model (Young et al., 2010). All other mixture properties like C_p, thermal conductivity, viscosity, mass diffusivity, and density are under ideal-gas mixing law, appropriate in a low pressure and high temperature thermal ALD reactor.

Momentum, mass, and energy transports are important in simulating the gas-phase velocity, temperature and concentration profile and in predicting the boundary profile at the wafer surface, which is used for the microscopic simulation. As mentioned before, ANSYS Fluent solves the coupled Navier–Stoke equations to obtain an accurate profile for the reactor dynamics. The following general flow field equations are given in the tensor form for Fluent calculations (Acton, 2012; Fluent, 2013):

$$\frac{\partial(\rho\vec{v})}{\partial t} + \nabla\cdot(\rho\vec{v}\vec{v}) = -\nabla P + \nabla\cdot(\bar{\bar{\tau}}) + \rho\vec{g} + \vec{F} \tag{1}$$

$$\bar{\bar{\tau}} = \mu\left[(\nabla\vec{v} + \nabla\vec{v}^T) - \frac{2}{3}\nabla\cdot\vec{v}I\right] \tag{2}$$

$$\frac{\partial}{\partial t}(\rho E) + \nabla(\vec{v}(\rho E + p)) = \nabla(k\nabla T - \Sigma h\vec{J} + (\bar{\bar{\tau}}\vec{v})) + S_h \tag{3}$$

$$\frac{\partial}{\partial t}(\rho Y_i) + \nabla\cdot(\rho\vec{v}Y_i) = -\nabla\cdot\vec{J}_i + R_i + S_i \tag{4}$$

$$\vec{J}_i = -\rho D_{m,i}\nabla Y_i - D_{T,i}\frac{\nabla T}{T} \tag{5}$$

where ρ is the density of the gas-phase species mixture, $\vec{v}$ is the velocity of gas-phase species mixture, P is the static pressure, T is the fluid temperature, $\vec{g}$ is the component of gravity on the direction of the fluid flow, $\bar{\bar{\tau}}$ is the stress tensor, μ is the fluid viscosity, E is the fluid internal energy, I is the unit tensor, R_i and S_i are the reactions and mass transfer source terms of species i, respectively, S_h is heat transfer source term, $\vec{J}_i$ is the diffusive flux of species i, and $D_{m,i}$ and $D_{T,i}$ are the mass and heat diffusivities of species i.

The operating pressure is set to be 133 Pa, which lies in the typical pressure range (100 ~ 500 mTorr) of thermal ALD processes (George, 2009). In the CFD model, the inlet of the reactor is defined as a mass-flow-inlet at 600 K and four UDFs are created to define the precursors half-cycle duration and fluxes, and the purging durations and fluxes according to experimental and industrial procedures (Granneman et al., 2007; King, 2011). The gas inlet temperature is specified to be 473.15 K according to the industrial standard (Lee et al., 2006). The outlet is defined as a pressure-outlet, simulating a 12 M^3/h rotary vacuum pump, and a UDF is used to specify a 1×10^{-5} mbar vacuum for the purging (Kääriäinen et al., 2013). The substrate plate temperature is maintained at 600 K with a simulated heater. The substrate surface, where the microscopic and macroscopic domain intersect, is defined as a mass-flow-outlet. Four UDFs are utilized to provide gas-phase boundary information for the microscopic model and to define the CFD boundary conditions, accounting for the consumption of precursors and the generation of side products from microscopic kMC deposition, which are characterized by the term S_i appearing in Eq. (4). However, the enthalpy exchange on the boundary, characterized by the term S_h in Eq. (3), is demonstrated to have minimal influence on the wafer temperature, and thus, it is not considered in our work. The information exchange and the interaction between the microscopic and macroscopic domains will be explained in more details in Section 2.5.

Based on the mesh structure introduced in the previous section, the finite volume method is utilized by ANSYS Fluent to solve the governing equations implicitly (Eymard et al., 2000). Specifically, for each time step, ANSYS Fluent adopts the pressure-based coupled algorithm to solve simultaneously the momentum, continuity, energy, species, and other transport equations. Calculations are iterated until the residual convergence criterions are satisfied.

The calculation time step and the courant number selection are also critical to the CFD simulation accuracy (Courant et al., 1967). Courant number is a quantitative description of the number of computational cells that the fluid moves through in one time step, where the time step is the unit discretization of the real physical time. The Courant-Friedrichs-Lewy (CFL) condition, a common criteria for finite-difference approximation of PDEs, relates the time step to the interval lengths in spatial coordinate and the speed of information traveling in the physical space (Moura and Kubrusly, 2012):

$$C = \frac{u\Delta t}{\Delta x} \tag{6}$$

where C is the selected courant number, Δx is the minimum cell length and u is the average flow velocity.

Traditional direct numerical PDE analysis allows a maximum courant number of 1, while the advanced CFD software allows convergence under higher courant number (Moura and Kubrusly, 2012). In particular, the Fluent pressure-based solver is less sensitive to courant number (Fluent, 2013). In our model,

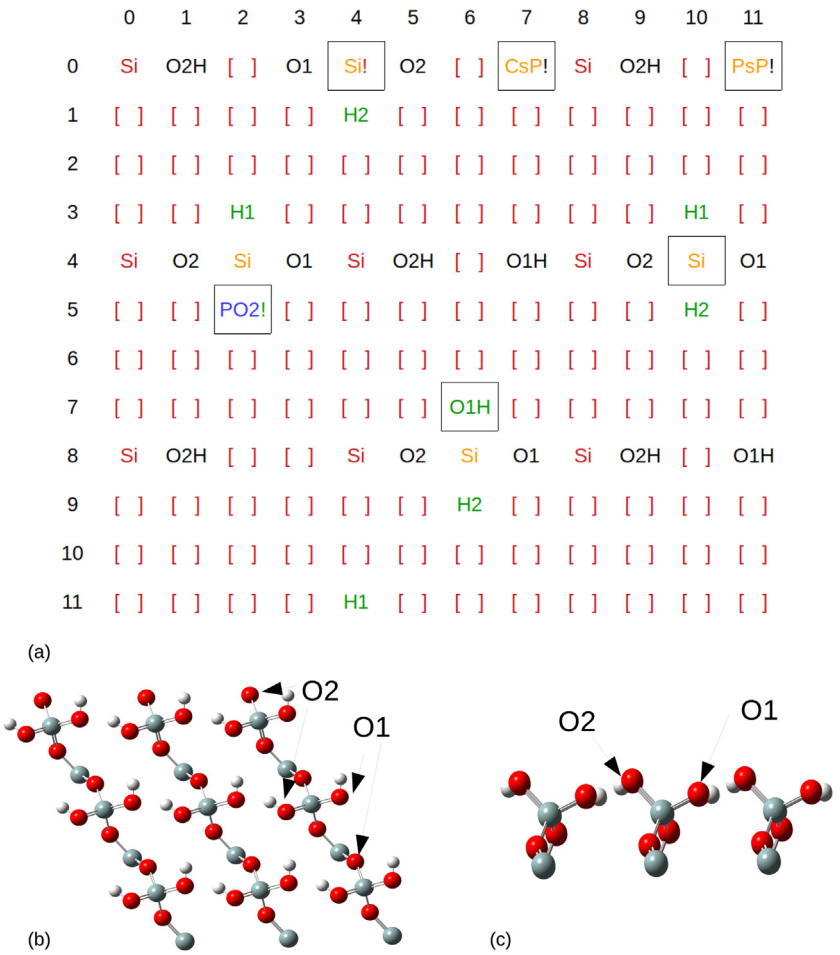

Fig. 3 – (a) Top view of a 5-layer 12 × 12-site miniature demonstration of the full kMC simulation lattice. The five layers and the species on the lattice are shown using different colors and symbols, respectively. The first (bottom) layer, labeled red, contains the base Si atoms. The second layer, labeled black, contains oxygen atoms or hydrogenated oxygens. The third layer, labeled yellow, contains the species from the first silicon half-cycle: Si is the neighbour-binding silicon, Si! is the self-binding silicon, and PsP and CsP are the physisorbed and chemisorbed precursors, respectively. The fourth layer, labeled green, contains the species from the first oxygen half-cycle: O and OH are the oxygen atoms and hydroxyl groups. The fifth (top) layer, labeled blue, contains physisorbed ozones (PO1 and PO2), which remain to be oxidized. (b) Top view of the hydroxylated SiO_2(001) surface. (c) Side view of the hydroxylated SiO_2(001) surface, where O1 is the more electronegative oxygen. The double bonds are due to Gaussian display format, which does not influence the validity of the structure. (For interpretation of the references to color in this figure legend, the reader is referred to the web version of this article).

a courant number of 50 is used, which proved to be able to converge the simulation efficiently, successfully and accurately. Using the above equation, time steps can be determined for the BTBAS half-cycle, purge, and ozone half-cycle depending on the different inlet flow rates, respectively. Time step sizes of 0.05 s and 0.01 s are used under 100 sccm and 1330 sccm BTBAS inlet flow rates, respectively. It was found that smaller time step sizes do not lead to significant change of the simulation accuracy, while bigger time steps lead to inaccurate results.

2.3. *Microscopic surface model*

Although the macroscopic CFD modeling determines the wafer surface boundary conditions (i.e., temperature and pressure of the surface chemistry), it does not provide any information about the behavior of the microscopic deposition regime. The microscopic simulation captures the structural detail of SiO_2 thin-film and the reaction mechanisms, which is modeled using 3D kMC algorithm. The 3D lattice assumption, detailed mechanism and kinetics for surface physical and chemical reactions, and the kMC formulation will be discussed in the following subsections.

2.3.1. *Structural assumptions of deposited SiO_2*

The α-Quartz SiO_2 thin-film has a local SiO_4 structure close to tetrahedron and a trigonal space group of $P3_121$. As demonstrated in Ding et al. (2019), a 3D triangular model is constructed as an approximation of the actual α-Quartz crystal structure. This approximation, Fig. 3(a), is a close resemblance of the real lattice, Fig. 3(b), and preserves the validity of the thin-film model. A final lattice dimension is 1200 × 1200 sites per layer with height dependent on the number of cycles simulated. This lattice is large enough to be size-independent while computationally efficient (Huang et al., 2010a,b).

2.3.2. *Reaction mechanism*

For each full deposition cycle in the ALD process, there are two half-cycles, each using a specific precursor species to deposit the desired element onto the film. As discussed in Section 2.1, BTBAS and ozone are chosen for the SiO_2 deposition simula-

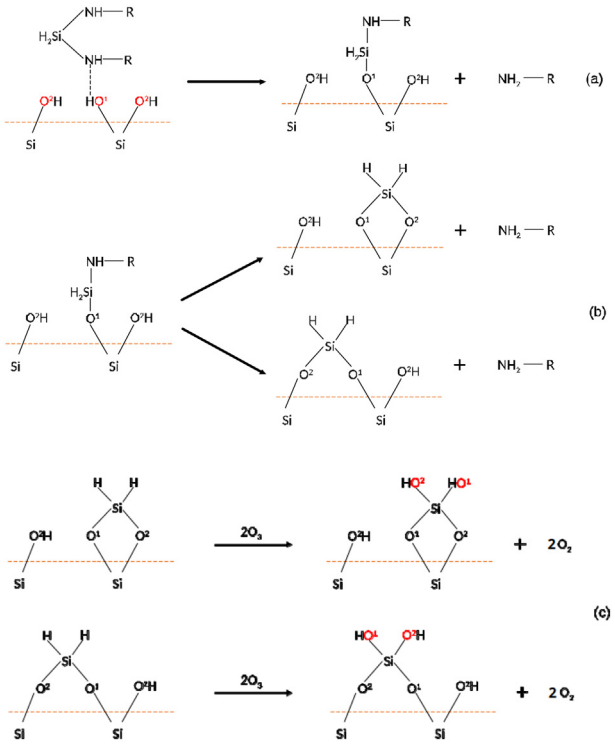

Fig. 4 – (a) First dissociative chemisorption step of BTBAS. (b) Second dissociative chemisorption step of BTBAS under self-binding and neighbour-binding mechanisms. (c) Oxidation of self-binding and neighbour-binding SiH_2 with ozone.

tion. The reaction mechanism using these two precursors was reported by Han et al. (2011) and is explained in detail below.

The first half-cycle is referred to as the Si-Cycle, which contains physisorption, abstraction and a two-step dissociative chemisorption. A hydroxylated SiO_2(001) substrate surface is defined as the basis, shown in Fig. 3(c). According to Han et al. (2011), the two oxygen atoms in a SiO_2 cell have different electronegativities. The more electronegative oxygen atom, denoted as O^1, is more reactive and is therefore more likely to be electrophilicity attacked by precursor particles than the less electronegative oxygen atom, denoted as O^2. Therefore, as shown in Fig. 4(a), the precursor particle is first physisorbed onto the O^1-type hydroxyl group through a strong H-bond to form the reactant. Then, the physisorbed precursor goes through the first dissociative chemisorption step, forming a monoamine intermediate and releasing one of the two aminoethyl groups. Next, the remaining aminoethyl group electrophilicity attacks an adjacent O^2-type hydroxyl group, which can be either from the neighbour Si atom, i.e., neighbour-binding route, or from the same substrate Si atom, i.e., self-binding route, as shown in Fig. 4(b). The former reaction pathway retains the original surface orientation, resulting in a thermodynamically favorable structure, whereas the latter, which is more kinetically favorable, causes a deviation from the (001) surface orientation and leads to defect formation. After the electrophilic attack, the other aminoethyl group is released from the surface structure and another O-Si bond is formed. The remaining two H atoms from the Si atom then become the new substrate surface. The competition of kinetic and thermodynamic favorability is crucial in explaining the structural non-uniformity of SiO_2. Therefore, both reaction pathways and their reverse reactions are incorporated in our kMC model, and the reaction kinetics will be explained in more details in the next section.

The second half-cycle is referred to as the O-Cycle, which contains the ozone physisorption, abstraction and surface oxidation. The oxidation steps of self-binding and neighbour-binding H-Si groups are shown in Fig. 4(c). Once the surface is partially/fully chemisorbed, both terminating H atoms will be oxidized by ozone to hydroxyl group (-OH), which are utilized in the next Si-cycle.

2.3.3. *Relative rate determination*

The reaction kinetic rates, discussed in the previous section, are important for kMC event selection. The physisorption is a gas-surface athermal barrierless process, and the Collision Theory, as expressed in the equation below, is generally used to determine the rate constant for such processes:

$$r_{phs} = \frac{p_i}{RT}\sqrt{\frac{8k_bT}{\pi m_i}}s_{c,i}N_a\sigma \tag{7}$$

where r_{phs} is the physisorption reaction rate, p_i is the partial pressure of the species i, R is the ideal gas constant, T is the temperature, k_b is the Boltzmann constant, m_i is the molecular weight of species i, $s_{c,i}$ is the sticking coefficient of the species i at given temperature, N_a is the Avogadro number, and σ is the average area per surface site. Although the sticking coefficient of BTBAS is not reported in previous works, we obtain its value through an analogy with the sticking coefficient of bis(diethylamino)silane (BDEAS) because of the structural and electronic similarity (Schwille et al., 2017c).

On the contrary, chemisorption, abstraction and oxidation are thermodynamically activated kinetic reactions, which are generally described by the transition state theory (TST) (Cortright and Dumesic, 2001). Assuming quasi-equilibrium is achieved between the complex and the reactant, the reaction rate can be estimated using the thermodynamic properties of the transition state complexes, which are computed using DFT. Thus, the reaction rate equation can be formulated with standard Arrhenius-type rate law as follows:

$$r_{rxn,i} = A_i\exp\left(\frac{-E_{a,i}}{k_bT}\right) \tag{8}$$

where $r_{rxn,i}$ is the reaction rate of the ith thermodynamically activated reaction, $E_{a,i}$ is its activation energy for the transition state complex, and A_i is its pre-exponential factor, which is determined as follows:

$$A_i = f_i^{TST}\left(\frac{k_bT}{h}\right) \tag{9}$$

where k_b is the Boltzmann constant, T is the temperature, and f_i^{TST} is the ratio of the vibrational partition function between the transition state complex and the reactant, calculated with DFT. In this work, all DFT calculations are performed using the Gaussian09 software, which will be illustrated in more details below. The resulting parameters are collected in Ding et al. (2019) and the associated nomenclature is explained in Section 2.3.4.

2.3.4. *Kinetic Monte Carlo algorithm*

As mentioned in the Introduction, a first-principles MD simulation is too computationally demanding to be feasible for the scale of system discussed in this work (Battaile and Srolovitz, 2002; Rey et al., 1991; Dkhissi et al., 2008). Thus, we adopt an

n-fold hybrid kMC algorithm in the framework proposed by earlier works (Lou and Christofides, 2004; Christofides et al., 2008; Crose et al., 2018). kMC is a stochastic algorithm that uses the kinetic rate information and uniformly distributed random numbers to determine event execution and system time evolution. Specifically, we define an event set as a collection of all events that have comparable rates. A total rate, r_{total}, is defined as:

$$r_{total} = \sum_{i=1}^{N} r_i \tag{10}$$

where r_i represents the respective rate of each event within an event set, which consists of total N events. Then, each rate is normalized with respect to the associated total rate to derive its relative probability. The normalized indicator of the ith event, $l_i \in (0, 1]$, can be interpreted as the sum of the normalized probabilities of the first i events:

$$l_i = \frac{\sum_{j=1}^{i} r_j}{r_{total}}, \quad i = 1, \ldots, N \tag{11}$$

This indicator is then used for event selection via a uniformly distributed random number selection, $\gamma_1 \in (0, 1]$. If γ_1 falls in the interval of normalized indicators l_{i-1} to l_i, the ith event will be selected for execution.

The transient behavior of the model is characterized by the time evolution scheme proposed by the kMC algorithm, where the amount of time for each event is governed by using another random number, $\gamma_2 \in (0, 1]$. Starting from a given time, the simulation time clock is advanced by Δt for the chosen event, where Δt is given by the following equation:

$$\Delta t = \frac{-\ln \gamma_2}{r_{total}} \tag{12}$$

Therefore, the total rate for O-Cycle is computed as follows:

$$r_{o,total} = r_{o,phs} + r_{o,des} + r_{o_a,f} + r_{o_b,f} \tag{13}$$

where $r_{o,phs}$ is the rate of ozone physisorption, $r_{o,des}$ is the rate of ozone desorption, and $r_{o_a,f}$ together with $r_{o_b,f}$ are the oxidation rates of the chemisorbed species attached to a neighbour-binding silicon. The oxidation rate of the chemisorbed species attached to a self-binding silicon is orders of magnitude higher than that of a neighbour-binding silicon. Therefore, it is considered instantaneous and deterministic, and thus, omitted in the O-Cycle kMC selection. Similarly, the total rate for Si-Cycle is:

$$r_{si,total} = r_{btbas,phs} + r_{btbas,des} + r_{neigh,f} + r_{neigh,r} + r_{self,f} + r_{self,r} \tag{14}$$

where $r_{btbas,phs}$ and $r_{btbas,des}$ are the physisorption and desorption rates of BTBAS, respectively. $r_{neigh,f}$ and $r_{neigh,r}$ are the forward and reverse rates of the neighbour-binding dissociative chemisorption, respectively, and $r_{self,f}$ and $r_{self,r}$ are the forward and reverse rates of the self-binding dissociative chemisorption, respectively. The reaction rate of first chemisorption step $r_{si,chem}$ is orders of magnitude higher than those of other events. Therefore, it is considered instantaneous and deterministic, and thus, omitted in the Si-Cycle kMC selection.

For the O-Cycle, the rates of all considered reactions are comparable and can be modeled with the standard n-fold kMC algorithm. However, for the Si-Cycle, in order to simulate the realistic behavior of reaction kinetics, we need to consider surface reaction events separately from physisorption events for the following two reasons: First, surface reaction events are formulated and compared differently from physisorption events since surface species concentrations need to be considered to correctly describe the competition between the thermodynamic and kinetic favorability of competing pathways. Second, physisorption rates are an order of magnitude lower than surface reaction rates according to the DFT calculation, which means that the model will be saturated by surface reactions events if the events are not allocated properly. Thus, a decoupled kMC scheme is proposed to partition the entire Si-Cycle events into two event sets: adsorption events containing only physisorption events, and surface reaction events containing the remaining events. The partitioned total rates, $r_{si,ads}$ and $r_{si,rxn}$, are then defined as follows:

$$r_{si,rxn} = r_{neigh,f} + r_{neigh,r} + r_{self,f} + r_{self,r} + r_{btbas,des} \tag{15}$$

$$r_{si,ads} = r_{btbas,phs} \tag{16}$$

Additionally, in order to apply the decoupling scheme, we first compute a ratio, $J_{si,ads}$ as the ratio of the adsorption rate versus the total rate, which is derived as follows:

$$J_{si,ads} = \frac{r_{si,ads}}{r_{si,total}} = 1 - J_{si,rxn} \tag{17}$$

Therefore, for a total assigned duration, t_{total}, adsorption events are pre-allocated with a duration of $t_{total} \cdot J_{si,ads}$, and the remaining time is assigned to surface reaction events. Next, during the allocated time period for surface reactions, the normalized event indicator under the competition of reaction pathways and directions is calculated by the concentration-weighted reaction rates as follows:

$$l_{si,i} = \frac{\sum_{j=1}^{i} r_{rxn,j} R_j}{\sum_{k=1}^{N} r_{rxn,k} R_k}, \quad i = 1, \ldots, N \tag{18}$$

where $l_{si,i} \in (0, 1]$ represents the normalized indicator of the ith event in the surface reaction event set, $r_{rxn,j}$ is the un-weighted chemical reaction rate for the jth event calculated from Eq. (8), R_j is the number of reactants for each surface reaction, and N is the total number of events in the Si-Cycle surface reaction event set. The normalized indicators are then used to execute the event selection following the same approach performed in the standard kMC algorithm. In Section 3, it is demonstrated that this decoupling scheme achieves desired accuracy.

2.4. DFT and thermodynamic calculations

The reaction mechanism along with the associated activation energies are reported for BTBAS and ozone for SiO_2 (Han et al., 2011). However, many fundamental thermodynamic properties of BTBAS are yet to be investigated. Since it is important for us to capture those thermodynamic properties to reproduce the correct behavior in both the macroscopic CFD model and the microscopic kMC model, DFT calculations are carried out using Gaussian09 software packages and parallel computational work with Linda worker is adopted (Frisch et al., 2000; Council et al., 2003; Fermeglia and Pricl, 2009; Liu and Liu, 2018).

2.4.1. Density functional theory

The solution of Schrödinger equation of many-body systems, as shown below, provides a first-principles understanding of the material properties (Jensen, 2017):

$$\hat{H}\Psi(r_i, R_I) = E\Psi(r_i, R_I) \tag{19}$$

where Ψ is the particle wave function, r_i is the position of each electron, R_i is the position of each nuclei, E is the ground state energy, and $\hat{H}$ is the Hamiltonian operator:

$$\hat{H} = \hat{T}_{nuc}(R) + \hat{V}_{coulomb} + \hat{H}_{elec}(r, R) \tag{20}$$

where $\hat{T}_{nuc}(R)$ is the nucleic kinetic energy, $\hat{V}_{coulomb}$ is the coulombic potential between nuclei and electrons, and $\hat{H}_{elec}(r, R)$ is the electronic Hamiltonian.

However, the exact solution to the Schrödinger equation of a many-body system is extremely difficult to obtain and its complexity scales rapidly with system size. Therefore, many efforts have been put to approximate the solution of the Schrödinger equation. DFT is one of those approaches, which, instead of focusing on each electron, solves for the overall electron density, $n(\mathbf{r})$ (Jensen, 2017). According to the Hohenberg and Kohn theorem, the ground state energy of the system is an unique functional of electron density (Gilbert, 1975). Therefore, by assuming the energy functional and minimizing the overall energy, the true electron density of the system can be obtained. The total energy functional consists of the non-interacting kinetic energy, electron-nuclei potential, the approximation of the full interaction (also known as the hartree energy), and the exchanges and correlations of the system (Gritsenko et al., 1997). The exact form of the exchange-correlation functional is not known and hence must be approximated. Over the past few decades, a lot of efforts have been made to propose highly-accurate energy functionals, with one of the most popular being the B3LYP (Becke, 3-parameters, Lee-Yang-Parr) functional (Lee et al., 1988; Becke, 1993). After having a descriptive energy functional, the overall system energy is broken down into the energies of pseudo spin-orbitals, known as the Kohn-Sham orbitals. The energy of each spin-orbitals is solved iteratively by reconciling the differences between the guessed electron density with the computed electron density from the proposed energy functional (Kohn and Sham, 1965). The final computation results for each Kohn-Sham orbitals are combined together to be an accurate electron density, which can then be used to compute a variety of material properties.

2.4.2. Macroscopic parameters determination

As mentioned in Section 2.2.2, BTBAS is not in the Fluent material database, and many physical and chemical properties that are crucial to thermodynamic calculations are not reported in previous works. Thus, its thermodynamic/physical parameters, including specific heat C_p, viscosity μ, standard state enthalpy of formation $\Delta_f H^\circ(M, 298\,K)$, and standard state entropy $S^\circ(298\,K)$, need to be computed for the gas-phase transport model. To determine those parameters, DFT calculations using the Gaussian-4 (G4) theory are performed. Based on ab-initio molecular-orbital theory, G4 is a precise computation method for calculating molecular energies of compounds composed of elements in the first three rows of the periodic table. Thus it is an appropriate and accurate method in determining the thermodynamic properties of BTBAS (Curtiss et al., 2007).

The method utilizes a sequence of single point energy calculations using appropriate basis set, spin-orbit correction and advanced higher level correction. The detailed calculation steps and energy corrections are discussed in literature (Curtiss et al., 2007). Using G4 method, standard state entropy $S^\circ(298\,K)$ and specific heat C_p of BTBAS under various temperatures can be directly calculated. The standard state enthalpy of formation $\Delta_f H^\circ(M, 298\,K)$ for the BTBAS molecule can be calculated from:

$$\Delta_f H^\circ(M, 298\,K) = \Delta_f H^\circ(M, 0\,K) + H^\circ_M(298\,K) - H^\circ_M(0\,K) - \sum_{atoms} x(H^\circ_X(298\,K) - H^\circ_X(0\,K)) \tag{21}$$

where $H^\circ_M(298\,K)$ is the molecular enthalpy at standard state and $H^\circ_M(0\,K)$ is the molecular enthalpy at 0 K. The difference between $H^\circ_M(298\,K)$ and $H^\circ_M(0\,K)$ accounts for the temperature correction on molecular enthalpy. Similarly, $\sum_{atoms} x(H^\circ_X(298\,K) - H^\circ_X(0\,K))$ is the enthalpy temperature correction of all atomic elements, given in Ochterski (2000), where X refers to each type of element and x is the number of element X. In addition, $\Delta_f H^\circ(M, 0\,K)$ is the enthalpy of formation of BTBAS molecule at 0 K, which is defined as:

$$\Delta_f H^\circ(M, 0\,K) = \sum_{atoms} x\Delta_f H^\circ(X, 0\,K) - \left(\sum_{atoms} x\epsilon_o(X) - \epsilon_0(M) - \epsilon_{ZPE}(M)\right) \tag{22}$$

where X refers to the type of each element, x is the number of X atom, $\Delta_f H^\circ(X, 0\,K)$ is the enthalpy of formation of element X at 0 K. Moreover, zero-point energy of molecule $\epsilon_{ZPE}(M)$, total energy of the molecule $\epsilon_0(M)$, and total energy of each atom $\epsilon_0(X)$ can be found directly from G4 method (Ochterski, 2000).

In addition, viscosity μ is estimated from the molecular theory of Newtonian gases, considering pure gas composed of rigid, non-attracting molecules, which is valid for low density scenario (Bird et al., 2007):

$$\mu = \frac{2}{3\pi}\frac{\sqrt{\pi mkT}}{\pi d^2} \tag{23}$$

where m is the molecular mass, k is the Boltzmann constant, T is the temperature, and d is the molecular diameter of the approximated rigid ball of BTBAS.

2.4.3. Microscopic parameters determination

For the surface reaction kinetics, many properties are difficult to measure experimentally yet essential to the accurate deposition simulation, including vibrational partition. As discussed in detail in Ding et al. (2019), in the Si-Cycle, to calculate properties of BTBAS and its reaction kinetics with SiO_2 lattice, the hydroxylated surface $3 \times 3 \times 1$ SiO_2 lattice is constructed and optimized to an acceptable energy minimum with basis set 6-31G+dp accuracy level (Lee et al., 1988; Becke, 1993; Frisch et al., 2000; Han et al., 2011; Mankad and Jhu, 2016). Subsequently, the TS complex is obtained from the optimized BTBAS molecule and a $3 \times 3 \times 1$ SiO_2 surface lattice, using optimization to transition state (Opt = TS) method with the same level of basis set accuracy. For the O-cycle, the same calculation procedure is implemented for the ozone molecule, H-Si surface lattice and physisorbed ozone. Finally, in order to perform a precise vibrational frequency calculation, the G4 method is

adopted. The vibrational partition function along with other important thermodynamic properties are reported in Ding et al. (2019).

2.5. Automated workflow and parallelization

In order to improve computational efficiency, parallelization and distribution of the calculations are adopted in the macroscopic and microscopic domains of the ALD reactor model, respectively. In the gas-phase domain, we utilized 36 cores on the UCLA Hoffman2 Cluster where the parallel computation is implemented by the Fluent message passing interface (MPI) (Fluent, 2013). The number of cores is chosen according to the parallel processing benchmark and the communication overhead between cores and the host node. Then, the output from the gas-phase model is passed to the microscopic model through an automatic workflow. To accurately represent the entire wafer surface, the substrate domain is spatially split into 36 sub-regions uniformly, each having a corresponding kMC model. Each kMC model runs in a serial manner, while the message passing interface distributes 36 distinct kMC models onto 36 idle cores on the cluster and manages the synchronization of all kMC models.

The interaction and methodology that connect the microscopic and the macroscopic domain are also crucial to the multiscale CFD model. In this study, the automated workflow adopted is shown in Fig. 1. The green region enclosed by dashed line belongs to the microscopic domain (kMC), the blue region belongs to the macroscopic domain (gas-phase), and the yellow region and the associated arrows belong to the cross-linkage. The simulation starts in the macroscopic domain at $t = 0$ where mass and energy balances are solved in the flow field in a time step Δt. Next, after the reconciliation of data between each computation node, the surface boundary conditions (e.g., temperature, partial pressure and time step) are collected for each sub-region and transferred to the microscopic domain. If the system is currently in a purge cycle, nothing will be done in the microscopic domain and it would continue with the macroscopic computation for the next time step. Otherwise, based on whether the system is in O-cycle or Si-cycle, the corresponding kMC algorithm will run to solve for the surface structure, reactions and precursor usage for a time interval Δt. After the computation, the results of all kMC sub-regions are synchronized, and then the averaged species fluxes for each sub-region are reported back to the macroscopic domain to update the corresponding boundary conditions for the next time step. The physical time of the system will be updated to $t + \Delta t$, according to an implicit Euler scheme (Fluent, 2013). If the current half-cycle has reached its assigned time limit at the end of the microscopic domain, the workflow scheme will inform the system to switch to the next half-cycle. This workflow is executed until the desired cycle number is achieved.

3. Multiscale CFD simulation results and chamber design

The results presented below represent the transient behavior of the thermal ALD reactor at operating conditions of $P = 133$ Pa and constant surface heating at $T = 600$ K, which are chosen according to the referenced experimental works and conventional industrial standard operating pressure and temperature of SiO_2 thermal ALD (Putkonen et al., 2014). The discussion mainly focuses on the BTBAS half-cycle, because the flow field of the purge and the ozone half-cycle behave similarly, and the major economic and processing time concerns are associated with BTBAS usage and throughput. The inlet BTBAS flow rate is one of the most important operating parameters, which varies from 100 sccm to 1330 sccm, and the half-cycle times are correspondingly adjusted according to the inlet flow rate, ranging from 5 s to 1 s, respectively. The maximum Knudsen number in all inlet flow rates is 0.096, an order of magnitude smaller than unity, which indicates that the continuum assumption in the flow conservation equations is valid and continuity-based CFD models can be utilized for the gas-phase simulation (Laurendeau, 2005). In the following sections, first, the nominal reactor design is tested and compared to literature and industrial inlet flow rates as a validation of the CFD model. Then, according to the simulation results, the non-ideal flow regime in the nominal design is identified, based on which the optimization of the showerhead and the design of reactor upstream configuration are carried out, respectively. Finally, the individual design improvements are integrated and adjusted to determine a final optimized design of the thermal ALD reactor.

3.1. Nominal geometry

The final coverage in all inlet conditions from 100 sccm to 1300 sccm are around 96–98%, corresponding to a growth per cycle (GPC) of 1.74–1.76 Å per cycle. The wafer cannot reach complete 100% full coverage because of insufficient cycle-time, competing reaction mechanism and equilibrium, but the GPC lies inside the range of the reported value of 1.4–2.1 Å per cycle, and this result is also consistent with the previously reported standalone kMC model results of 1.8 Å (O'Neill et al., 2011; Ding et al., 2019). At an inlet flow rate of 1330 sccm, the gas-phase development takes 0.5 s to reach steady-state and, as shown in Fig. 5, the entire wafer reaches steady-state coverage at 1.06 s, which is very close to the experimentally determined cycle time interpolated at the same operating conditions and reactor design, which is 0.931 s (Granneman et al., 2007). In the industrial process, the precursor flow rate is lower due to economic concern, and a typical choice of flow rate is within 50 to 100 sccm, along with a standard half-cycle time of 5 s. For our model, at an inlet flow rate of 100 sccm, the gas-phase development has reached steady-state in 5.8 s cycle time, with an average wafer coverage close to the desired unity value. Also, the importance of the interconnection between microscopic and macroscopic domain is demonstrated. Several trials of standalone CFD and consecutive standalone kMC simulation are carried out, with no updated boundary surface precursor consumption from kMC to CFD on the wafer surface. A transient differences of 10–20% in surface partial pressure, deposition rate and cycle-time are observed. These significant deviations show that the application of the interchange of information and the multiscale workflow is critical to the accuracy of ALD process simulation. Therefore, our multiscale CFD model is a good representation of the realistic full thermal ALD reactor, and the nominal reactor design at 100 sccm inlet flow rate will be used as a base case for reactor design optimization below.

As shown in Fig. 5, the transient thin-film growth in the peripheral region (radius >120 mm) of the wafer is the fastest, and the transient thin-film growth in the central region (radius <70 mm) is the slowest. The maximal transient deposition rate discrepancy at a single time step is more than 400%. Since the surface temperature is maintained to be uniform

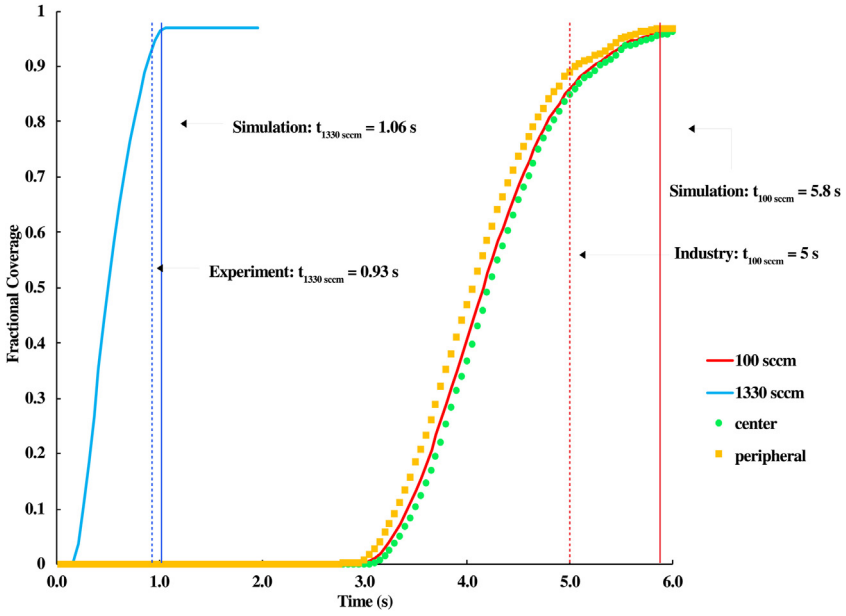

Fig. 5 – Transient deposition rates at inlet flows of 100 sccm and 1330 sccm. The *y*-axis is the fractional coverage, and the *x*-axis is the deposition time. The dashed blue and red lines are the experimental or industrial referenced cycle times at 1330 sccm and 100 sccm, respectively. The vertical blue and red lines are the simulation steady-state cycle times at 1330 sccm and 100 sccm, respectively. The blue and red solid curves are average deposition rates at 1330 sccm and 100 sccm, respectively. The yellow and green data points are the deposition rates of the peripheral and the center region, respectively. (For interpretation of the references to color in this figure legend, the reader is referred to the web version of this article).

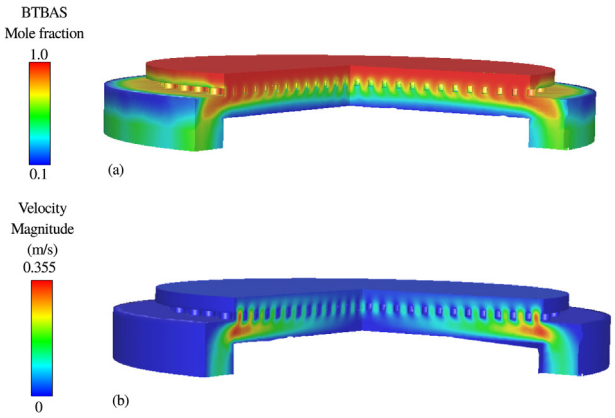

Fig. 6 – BTBAS mole fraction distribution and velocity flow field of the nominal design for inlet flow rate at 100 sccm. (a) A 3D view of the BTBAS development in the entire reactor scale at half standard Si-cycle time (2.5 s). (b) A 3D view of the velocity profile in the entire reactor scale at half standard Si-cycle time (2.5 s).

by a surface heater, this large transient non-uniformity in the deposition speed is directly caused by the uneven distribution of BTBAS partial pressure on the wafer surface. This partial pressure non-uniformity is associated with the velocity profile in the reactor upstream. Because the gas flow outlet is located around the wafer, the higher local dynamic pressure difference speeds up the flow near the reactor side wall. Thus, the flow velocity close to the reactor side wall is much higher and the gas flow stagnates in a temporary dead zone in the central region, shown in Fig. 6(b). As a result, BTBAS particles reach the outer part of the wafer much faster than the central region, as shown in Fig. 6(a). Therefore, even though the total pressure does not vary much on the wafer surface, the partial pressure of the precursor is lower in the center of the wafer region.

3.2. *Improved reactor chamber design*

In this section, we will discuss the progressive optimization of the ALD reactor geometry. As shown in the previous section, the initial attempt to use a nominal geometry of the showerhead ALD reactor design fails to provide a uniform and fast flow field development. The non-uniformity issue is reduced using the radially adaptive adjustment of the size and position of showerhead holes. Also, an actual inlet is added to the reactor model, and then the upstream region is modified as a volume adjusting horn, described by US Patent (Lee et al., 2006), which decreases the upstream deadzone volume and guides the precursor stream towards more uniform distribution downstream. The gas-phase simulation adopting each design improvement is analyzed and a final design that adjusts and combines those two aspects of optimization will be examined.

3.2.1. *Showerhead design development*

In the nominal design of the showerhead, shown in Fig. 7(a), there are 449 showerhead holes uniformly spaced in an orthogonal manner throughout the entire showerhead panel, which is 340 mm in diameter. Each showerhead hole has a diameter of 10 mm, and the radial distance between two showerhead holes is about 4 mm. However, as demonstrated in the previous section, this evenly distributed showerhead panel is not able to generate a uniform flow field because of the overall reactor spatial geometry.

In order to resolve the non-uniformity in the mass flow rate profile throughout the showerhead, the size and distribution of the showerhead holes can be redesigned so that the mass flow rate in the central region and the peripheral regions are balanced. First, the relationship between hole size and mass flow rate must be understood. For an ideal fluid flowing through a frictionless hole, a smaller hole diameter would speed up the fluid to keep the volumetric flow rate constant.

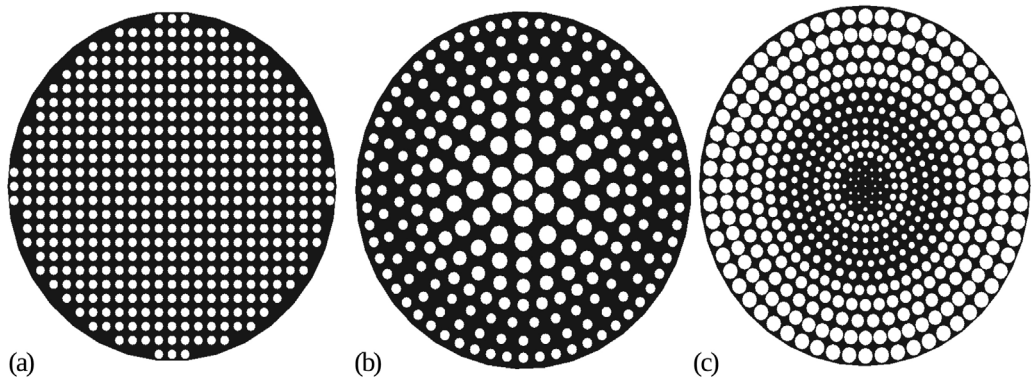

Fig. 7 – Nominal and modified showerhead designs. (a) Shows the industrial standard orthogonal showerhead distribution. (b) Shows the radially modified showerhead design for the well-developed inlet reactor. (c) Shows the radially optimized showerhead design for the final reactor design with a small inlet and a modified upstream.

However, a realistic flow field with complex geometry demonstrates that there is a large dependence on friction. According to the Hagen-Poiseuille equation, which is valid for describing the friction of a small-diameter tube under a flow regime with Re <20, a smaller diameter would induce a much larger friction loss:

$$S = \frac{32\mu v}{gD^2} \tag{24}$$

where S is the hydraulic slope (head loss due to friction), μ is the dynamic viscosity, v is the velocity and, g is the gravitational acceleration, and D is the diameter of each showerhead hole. This friction loss lowers the local differential pressure, hence slowing down the flow through the hole. Thus, the actual volumetric flow rates through the smaller holes are much lower than those of the bigger holes. Nevertheless, the dynamic pressure across the entire wafer is complicated and the exact showerhead hole size and distribution are adjusted run-to-run according to the CFD simulation results.

A modified radially distributed showerhead design shown in Fig. 7(b) is developed to improve the nominal reactor geometry. In total, 233 showerhead holes are deployed throughout the panel, where the diameter of showerhead holes in the central region is 20 mm and the diameter radially decreases to 10 mm at the periphery. As shown in Fig. 8(a), the modified showerhead allows a more radially uniform flow field distribution across the showerhead holes with all the other operating conditions being the same. In addition, Fig. 8(b) and (c) demonstrate that the partial pressure on the substrate surface has less radial variation and is able to reach almost unity everywhere at steady-state. Thus, a larger showerhead hole indeed leads to a higher mass flow in the corresponding downstream region. However, this modification has a disadvantage that the substrate species distribution has an azimuthal pattern, which was resulted from the linearly arranged showerhead holes at each 60 degree angle. Therefore, this method of showerhead optimization will be further adjusted for the final design of the ALD reactor after incorporating the upstream modification.

3.2.2. *Upstream geometry improvement*

In the nominal design, the inlet region is assumed to be a fully developed flow field. However, in a realistic industrial ALD reactor, the precursor gas enters the reactor chamber through a narrow gas inlet that is around 10 mm in diameter, located close to the showerhead, in order to reduce the time and precursor usage for developing a steady flow profile (Lee et al., 2006). Thus, instead of assuming a well-developed inlet region, we add the actual small inlet at the reactor top in our model to reflect realistic industrial scenario. Although the smaller and lower inlet can reduce the time of gas profile development, the sudden expansion leads to undesirable flow turbulence around the inlet and a confined vertical gas flow as shown in Fig. 9(a).

A reasonable solution is to add a physical component, a volume adjusting horn, in the dead zone of the upstream region after the small inlet to reduce the discharge coefficient and to guide the velocity and pressure profiles towards the peripheral region, as shown in Fig. 9(b) and (d) (Lee et al., 2006). The simulation results from Fig. 9(a) and (b) demonstrate that the inlet turbulence is reduced to a great extent, preventing possible damage of the deposited film. In addition, Fig. 9(c) and (d) show that the gas stream tends to flow vertically after it enters the reactor chamber, and the horn-shaped upstream configuration successfully generates more radial momentum so that region far away from the center can have an increased mass flow. Thus, this canopy-like upstream chamber wall facilitates the radial motion of gas stream, reduces undesirable inlet disturbance and allows for more uniform velocity and precursor partial pressure development.

3.2.3. *Integrated optimal ALD chamber design and evaluation*

According to the individual optimizations introduced in the previous sections, the transient flow non-uniformity could be mitigated by changing the sizes of showerhead holes as well as their locations. In general, larger holes lead to higher volumetric flow rate. The actual small inlet represents the realistic industrial reactor geometry, and reduces gas-phase development time. The canopy-like upstream chamber decreases dead zone volume and enhances radial flow. Therefore, in order to reduce the ALD cycle time, the final design should consider all aforementioned geometry optimizations and fine-tune them to achieve the optimal result.

The final ALD reactor design combines the small inlet, the modified upstream region introduced in the last section, shown in Fig. 9(b), and the optimized showerhead holes distribution, shown in Fig. 7(c). Although it is demonstrated that a confined flow can lead to a faster gas-phase development, the high velocity (>30 m/s) of the confined gas stream could potentially cause showerhead fouling and damage to the deposited film and long-term contamination of the showerhead holes. The high speed stream, possibly combined with radicals from

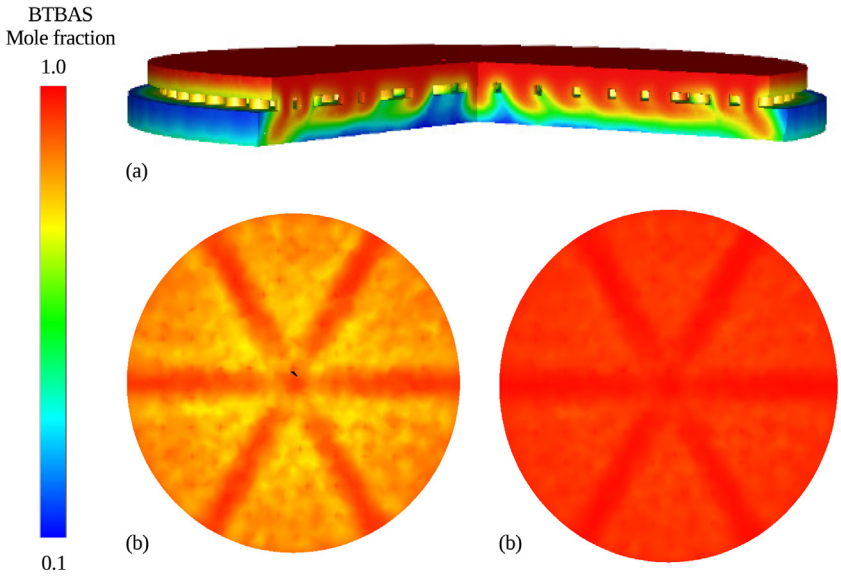

Fig. 8 – BTBAS mole fraction distribution of the radially adjusted showerhead design for 100 sccm inlet flow rate. (a) Shows a 3D view of the modified showerhead region. (b) and (c) show the transient profile and the steady-state profile of the substrate surface, respectively.

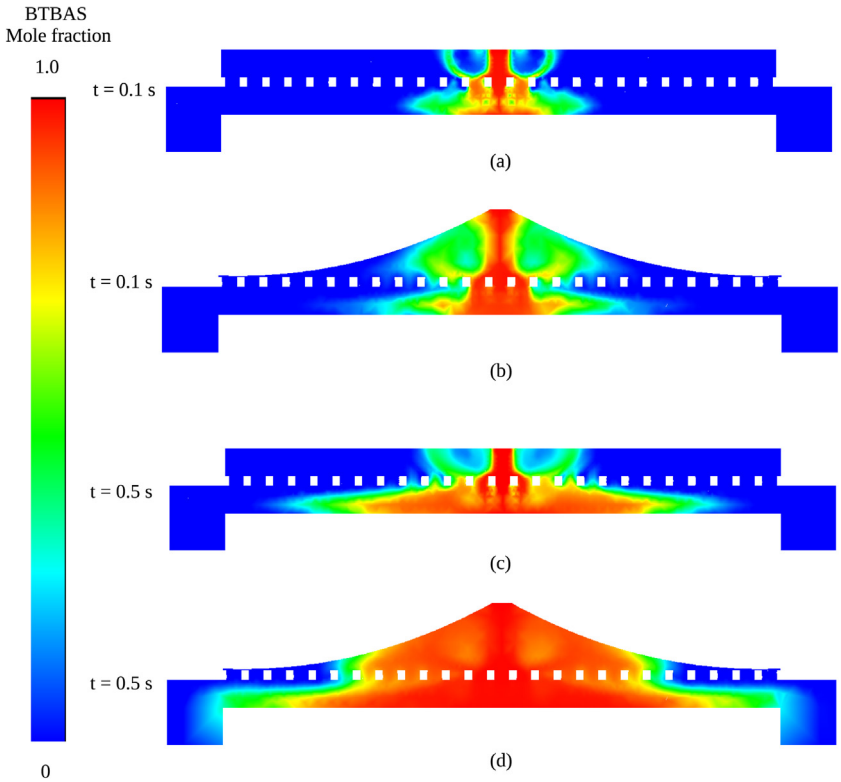

Fig. 9 – BTBAS mole fraction comparison of the modified upstream design and the sudden small inlet design for 100 sccm inlet flow rate. (a) and (c) show the sudden inlet design at 0.5 s and 1 s respectively. (b) and (d) show the modified upstream design at 0.5 s and 1 s, respectively.

plasma treatment, will have enough bombardment energy that is destructive to the deposited wafer surface. Therefore, in this design, the central region of the showerhead panel contains small holes that are 5 mm in diameter to prevent the direct mass flow onto the substrate surface and enhance radial dispersion. The holes immediately around the central region are much bigger in order to reduce the turbulence and to compensate for the low downward dynamic pressure caused by the turbulence, and the outer showerhead holes are radially increased according to the velocity profile.

As shown in Fig. 10(a), the species mass transfer is much more uniform radially across the entire wafer and is causing less turbulence than that in Fig. 9(d). The small showerhead holes in the middle of the showerhead successfully reduce the gas velocity right below the inlet area, while the horn-shaped upstream and the bigger holes, together, create higher differential pressure gradient towards the side of the reactor, hence increasing the radial velocity. As a result, the species development across the showerhead holes and wafer surface are acceptably uniform, as shown in Fig. 10(b) and (c). In addition,

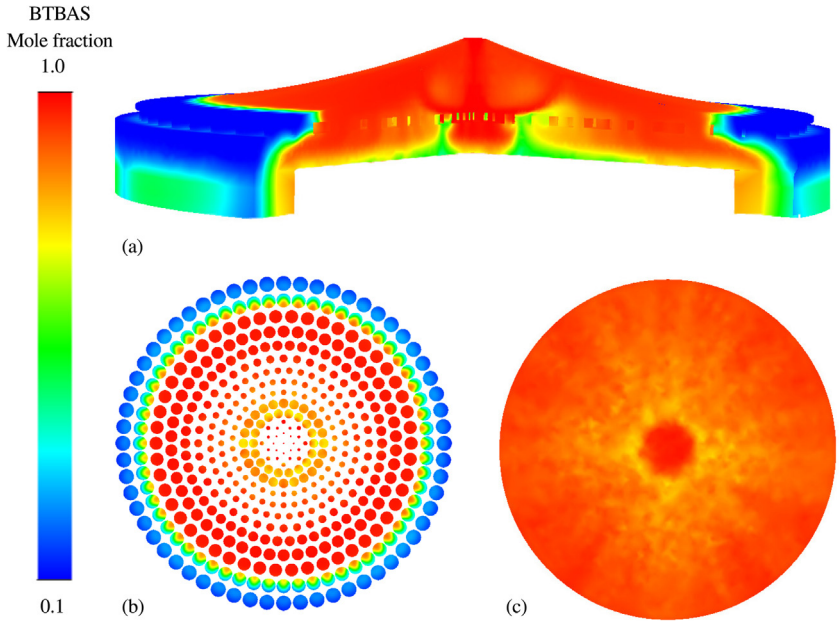

Fig. 10 – BTBAS mole fraction distribution of the final reactor design at 1.25 s for 100 sccm inlet flow rate. (a) Shows the 3D view of the entire reactor. (b) shows the z-cross-section view at the middle of the showerhead. (c) Shows the wafer surface.

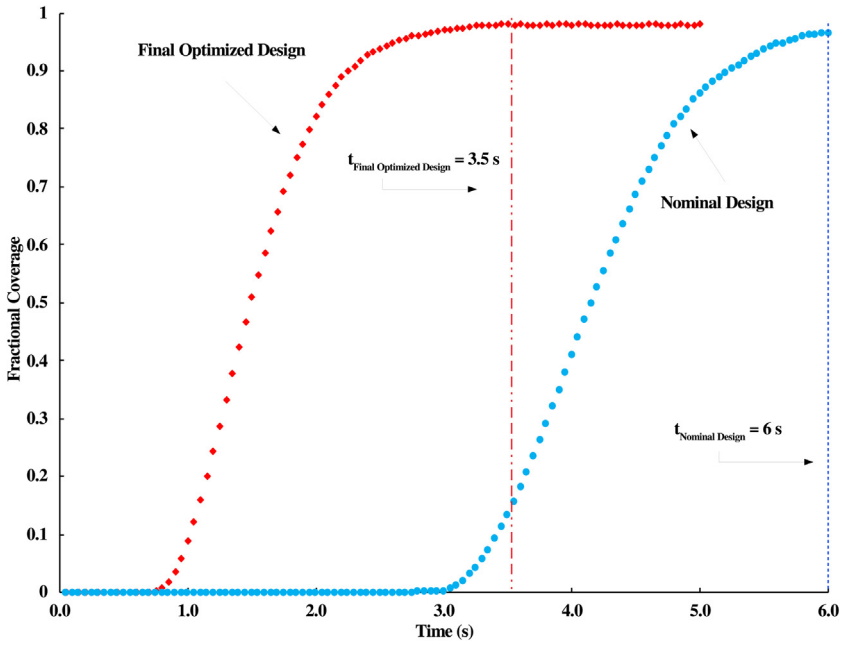

Fig. 11 – Transient deposition rate comparison of the nominal design and the final optimized design. The y-axis is the fractional coverage, and the x-axis is the deposition time. The red data points and dashed line are the transient fractional coverage and the steady-state cycle time of the optimized reactor design, respectively. The blue data points and dashed line are the transient fractional coverage and the steady-state cycle time of the nominal reactor design, respectively. (For interpretation of the references to color in this figure legend, the reader is referred to the web version of this article).

it is shown in Fig. 11 that the optimized final design leads to a 39.6% shorter finishing time for BTBAS half-cycle.

4. Conclusion

In this work, we developed a first-principles-based multi-scale 3D CFD model of thermal ALD of SiO_2 thin-films using BTBAS and ozone as precursors. Application of this model for a nominal reactor geometry design successfully reproduced experimental and industrial GPC and half-cycle time at 100 sccm and 1330 sccm precursor inlet flow rates. Based on the transient non-uniformity discovered in the nominal design, geometry optimizations on the showerhead hole size and distribution and upstream region were performed and their influence on the gas-phase profile and microscopic deposition were investigated. Two geometry optimizations were adjusted and combined for a final optimized design of the ALD showerhead reactor. The resulting optimal chamber design successfully reduced the gas-phase profile development time and created radial momentum that guided the gas stream to the less concentrated region. As a result, under the same industrial standard operating conditions, the optimized geometries reduced the half-cycle time by 39.6%, while maintaining a GPC of 1.76 Å per cycle. Moreover, the multiscale

simulation methodology developed in this paper can serve as a guidance model to other ALD systems where gas-phase transport and surface deposition need different simulation methods with information exchange. With the correct reaction kinetics for the microscopic film growth model and thermodynamic data of the reactants and products for the macroscopic gas transport model, such multiscale model can realistically represent a variety of ALD processes. In our future work, we are going to delve into the connections between the operating conditions and the cycle-time needed and to build a data-driven model to characterize such complex relationship. This model will systematically reflect the influences of the operating temperatures, pressures and flow rates, and also will help experimental and industrial works select and control ALD parameters more effectively and efficiently.

Acknowledgments

Financial support from the National Science Foundation is gratefully acknowledged.

References

Acton, Q.A., 2012. Chemical Processes-Advances in Research and Application: 2012 Edition: ScholarlyBrief. ScholarlyEditions.

Battaile, C.C., Srolovitz, D.J., 2002. Kinetic Monte Carlo simulation of chemical vapor deposition. Annu. Rev. Mater. Res. 32, 297–319.

Becke, A.D., 1993. Density-functional thermochemistry. III. The role of exact exchange. J. Chem. Phys. 98, 5648–5652.

Bird, R.B., Stewart, W.E., Lightfoot, E.N., 2007. Transport Phenomena. John Wiley & Sons.

Bühler, J., Steiner, F., Baltes, H., 1997. Silicon dioxide sacrificial layer etching in surface micromachining. J. Micromech. Microeng. 7, R1.

Chaffart, D., Ricardez-Sandoval, L.A., 2017. Robust dynamic optimization in heterogeneous multiscale catalytic flow reactors using polynomial chaos expansion. J. Process Control 60, 128–140.

Chaffart, D., Ricardez-Sandoval, L.A., 2018. Optimization and control of a thin film growth process: a hybrid first principles/artificial neural network based multiscale modelling approach. Comput. Chem. Eng. 119, 465–479.

Christofides, P.D., Armaou, A., Lou, Y., Varshney, A., 2008. Control and Optimization of Multiscale Process Systems. Springer Science & Business Media.

Cortright, R.D., Dumesic, J.A., 2001. Kinetics of heterogeneous catalytic reactions: analysis of reaction schemes. Adv. Catal. 46, 161–264.

Council, N.R., et al., 2003. Beyond the Molecular Frontier: Challenges for Chemistry and Chemical Engineering. National Academies Press.

Courant, R., Friedrichs, K., Lewy, H., 1967. On the partial difference equations of mathematical physics. IBM J. Res. Dev. 11, 215–234.

Crose, M., Kwon, J.S.I., Nayhouse, M., Ni, D., Christofides, P.D., 2015. Multiscale modeling and operation of PECVD of thin film solar cells. Chem. Eng. Sci. 136, 50–61.

Crose, M., Zhang, W., Tran, A., Christofides, P.D., 2018. Multiscale three-dimensional CFD modeling for PECVD of amorphous silicon thin films. Comput. Chem. Eng. 113, 184–195.

Curtiss, L.A., Redfern, P.C., Raghavachari, K., 2007. Gaussian-4 theory. J. Chem. Phys. 126, 084108.

Dalton, T.J., Conner, W.T., Sawin, H.H., 1994. Interferometric real-time measurement of uniformity for plasma etching. J. Electrochem. Soc. 141, 1893–1900.

Ding, Y., Zhang, Y., Kim, K., Tran, A., Wu, Z., Christofides, P.D., 2019. Microscopic modeling and optimal operation of thermal atomic layer deposition. Chem. Eng. Res. Des. 145, 159–172.

Dkhissi, A., Estève, A., Mastail, C., Olivier, S., Mazaleyrat, G., Jeloaica, L., Djafari-Rouhani, M., 2008. Multiscale modeling of the atomic layer deposition of HfO_2 thin film grown on silicon: how to deal with a kinetic Monte Carlo procedure. J. Chem. Theory Comput. 4, 1915–1927.

Elam, J., Groner, M., George, S., 2002. Viscous flow reactor with quartz crystal microbalance for thin film growth by atomic layer deposition. Rev. Sci. Instrum. 73, 2981–2987.

Elliott, S.D., Greer, J.C., 2004. Simulating the atomic layer deposition of alumina from first principles. J. Mater. Chem. 14, 3246–3250.

Eymard, R., Gallouët, T., Herbin, R., 2000. Finite volume methods. Handbook of Numerical Analysis, vol. 7., pp. 713–1018.

Fermeglia, M., Pricl, S., 2009. Multiscale molecular modeling in nanostructured material design and process system engineering. Comput. Chem. Eng. 33, 1701–1710.

Fluent, A., 2013. ANSYS Fluent Theory Guide 15.0. ANSYS, Canonsburg, PA.

Foong, T.R.B., Shen, Y., Hu, X., Sellinger, A., 2010. Template-directed liquid ALD growth of TiO_2 nanotube arrays: properties and potential in photovoltaic devices. Adv. Funct. Mater. 20, 1390–1396.

Frisch, A., Nielsen, A.B., Holder, A.J., 2000. Gaussview User Manual. Gaussian Inc., Pittsburgh, PA, pp. 556.

George, S.M., 2009. Atomic layer deposition: an overview. Chem. Rev. 110, 111–131.

George, S.M., Ott, A.W., Klaus, J.W., 1996. Surface chemistry for atomic layer growth. J. Phys. Chem. 100, 13121–13131.

Gilbert, T., 1975. Hohenberg-Kohn theorem for nonlocal external potentials. Phys. Rev. B 12, 2111.

Granneman, E., Fischer, P., Pierreux, D., Terhorst, H., Zagwijn, P., 2007. Batch ALD: characteristics, comparison with single wafer ALD, and examples. Surf. Coat. Technol. 201, 8899–8907.

Gritsenko, O.V., Schipper, P.R.T., Baerends, E.J., 1997. Exchange and correlation energy in density functional theory: comparison of accurate density functional theory quantities with traditional hartree-fock based ones and generalized gradient approximations for the molecules Li_2, N_2, N_2. J. Chem. Phys. 107, 5007–5015.

Han, B., Zhang, Q., Wu, J., Han, B., Karwacki, E.J., Derecskei, A., Xiao, M., Lei, X., O'Neill, M.L., Cheng, H., 2011. On the mechanisms of SiO_2 thin-film growth by the full atomic layer deposition process using bis(t-butylamino)silane on the hydroxylated SiO_2(001) surface. J. Phys. Chem. C 116, 947–952.

Huang, J., Hu, G., Orkoulas, G., Christofides, P.D., 2010a. Dependence of film surface roughness and slope on surface migration and lattice size in thin film deposition processes. Chem. Eng. Sci. 65, 6101–6111.

Huang, J., Hu, G., Orkoulas, G., Christofides, P.D., 2010b. Dynamics and lattice-size dependence of surface mean slope in thin-film deposition. Ind. Eng. Chem. Res. 50, 1219–1230.

Ishikawa, K., Karahashi, K., Ichiki, T., Chang, J.P., George, S.M., Kessels, W., Lee, H.J., Tinck, S., Um, J.H., Kinoshita, K., 2017. Progress and prospects in nanoscale dry processes: how can we control atomic layer reactions? Jpn. J. Appl. Phys. 56, 06HA02.

Jensen, F., 2017. Introduction to Computational Chemistry. John Wiley & Sons.

Kääriäinen, T., Cameron, D., Kääriäinen, M.L., Sherman, A., 2013. Atomic Layer Deposition: Principles, Characteristics, and Nanotechnology Applications. John Wiley & Sons.

King, S.W., 2011. Plasma enhanced atomic layer deposition of SiN_x:H and SiO_2. J. Vac. Sci. Technol. A: Vac. Surf. Films 29, 041501.

Knoops, H.C.M., Langereis, E., Van De Sanden, M.C.M., Kessels, W.M.M., 2010. Conformality of plasma-assisted ALD: physical processes and modeling. J. Electrochem. Soc. 157, G241–G249.

Kohn, W., Sham, L.J., 1965. Self-consistent equations including exchange and correlation effects. Phys. Rev. 140, A1133–A1138.

Kwon, J.S.I., Nayhouse, M., Orkoulas, G., Ni, D., Christofides, P.D., 2015a. A method for handling batch-to-batch parametric drift using moving horizon estimation: Application to run-to-run mpc of batch crystallization. Chem. Eng. Sci. 127, 210–219.

Kwon, J.S.I., Nayhouse, M., Orkoulas, G., Ni, D., Christofides, P.D., 2015b. Run-to-run-based model predictive control of protein crystal shape in batch crystallization. Ind. Eng. Chem. Res. 54, 4293–4302.

Laurendeau, N.M., 2005. Statistical Thermodynamics: Fundamentals and Applications. Cambridge University Press.

Lee, C., Yang, W., Parr, R.G., 1988. Development of the colle-salvetti correlation-energy formula into a functional of the electron density. Phys. Rev. B 37, 785.

Lee, C.S., Oh, M.S., Park, H.S., 2006. Plasma enhanced atomic layer deposition (PEALD) equipment and method of forming a conducting thin film using the same thereof. US Patent 7,138,336.

Liu, Y., Liu, H., 2018. Development of 3D polymer DFT and its application to molecular transport through a surfactant-covered interface. AIChE J. 64, 238–249.

Lou, Y., Christofides, P.D., 2004. Feedback control of surface roughness of GaAs(001) thin films using kinetic Monte Carlo models. Comput. Chem. Eng. 29, 225–241.

Mankad, V., Jhu, P.K., 2016. First-principles study of water adsorption on α-SiO_2(110) surface. AIP Adv. 6, 085001.

Moura, C.A.D., Kubrusly, C.S., 2012. The Courant-Friedrichs-Lewy (CFL) Condition: 80 Years After Its Discovery. Birkhäuser Basel.

Murray, C.A., Elliott, S.D., Hausmann, D., Henri, J., LaVoie, A., 2014. Effect of reaction mechanism on precursor exposure time in atomic layer deposition of silicon oxide and silicon nitride. ACS Appl. Mater. Interfaces 6, 10534–10541.

Nalwa, H. (Ed.), 2002. Handbook of Thin Films, vol. 1. Academic Press, Burlington.

Nishiguchi, T., Nonaka, H., Ichimura, S., Morikawa, Y., Kekura, M., Miyamoto, M., 2002. High-quality SiO_2 film formation by highly concentrated ozone gas at below 600°C. Appl. Phys. Lett. 81, 2190–2192.

Ochterski, J.W., 2000. Thermochemistry in Gaussian. Gaussian Inc., pp. 1–19.

Oh, S.K., Lee, J.M., 2016. Iterative learning model predictive control for constrained multivariable control of batch processes. Comput. Chem. Eng. 93, 284–292.

O'Neill, M.L., Bowen, H.R., Derecskei-Kovacs, A., Cuthill, K.S., Han, B., Xiao, M., 2011. Impact of aminosilane precursor structure on silicon oxides by atomic layer deposition. Electrochem. Soc. Interface 20, 33–37.

Pan, D., Li, T., Chien Jen, T., Yuan, C., 2014. Numerical modeling of carrier gas flow in atomic layer deposition vacuum reactor: a comparative study of lattice Boltzmann models. J. Vac. Sci. Technol. A: Vac. Surf. Films 32, 01A110.

Pittal, S., Snyder, P.G., Ianno, N.J., 1993. Ellipsometry study of non-uniform lateral growth of ZnO thin films. Thin Solid Films 233, 286–288.

Prechtl, G., Kersch, A., Icking-Konert, G.S., Jacobs, W., Hecht, T., Boubekeur, H., Schröder, U., 2003. A model for Al_2O_3 ALD conformity and deposition rate from oxygen precursor reactivity. In: Proceedings of the International Electron Devices Meeting, Washington, DC, USA.

Putkonen, M., Bosund, M., Ylivaara, O.M., Puurunen, R.L., Kilpi, L., Ronkainen, H., Sintonen, S., Ali, S., Lipsanen, H., Liu, X., 2014. Thermal and plasma enhanced atomic layer deposition of SiO_2 using commercial silicon precursors. Thin Solid Films 558, 93–98.

Rasoulian, S., Ricardez-Sandoval, L.A., 2015. Robust multivariable estimation and control in an epitaxial thin film growth process under uncertainty. J. Process Control 34, 70–81.

Rasoulian, S., Ricardez-Sandoval, L.A., 2016. Stochastic nonlinear model predictive control applied to a thin film deposition process under uncertainty. Chem. Eng. Sci. 140, 90–103.

Rey, J.C., Cheng, L., McVittie, J.P., Saraswat, K.C., 1991. Monte Carlo low pressure deposition profile simulations. J. Vac. Sci. Technol. A 9, 1083–1087.

Schuegraf, K., Abraham, M.C., Brand, A., Naik, M., Thakur, R., 2013. Semiconductor logic technology innovation to achieve sub-10 nm manufacturing. IEEE J. Electron Dev. Soc. 1, 66–75.

Schwille, M.C., Barth, J., Schössler, T., Schön, F., Bartha, J.W., Oettel, M., 2017a. Simulation approach of atomic layer deposition in large 3D structures. Model. Simul. Mater. Sci. Eng. 25, 035008.

Schwille, M.C., Schössler, T., Barth, J., Knaut, M., Schön, F., Höchst, A., Oettel, M., Bartha, J., 2017b. Experimental and simulation approach for process optimization of atomic layer deposited thin films in high aspect ratio 3D structures. J. Vac. Sci. Technol. A: Vac. Surf. Films 35, 01B118.

Schwille, M.C., Schössler, T., Florian, S., Oettel, M., Bartha, J.W., 2017c. Temperature dependence of the sticking coefficients of bis-diethyl aminosilane and trimethylaluminum in atomic layer deposition. J. Vac. Sci. Technol. A: Vac. Surf. Films 35, 01B119.

Shirazi, M., Elliott, S.D., 2014. Atomistic kinetic Monte Carlo study of atomic layer deposition derived from density functional theory. J. Comput. Chem. 35, 244–259.

Tanner, C.M., Perng, Y.C., Frewin, C., Saddow, S.E., Chang, J.P., 2007. Electrical performance of Al_2O_3 gate dielectric films deposited by atomic layer deposition on 4*H*-SiC. Appl. Phys. Lett. 91, 203510.

Tran, A., Aguirre, A., Durand, H., Crose, M., Christofides, P.D., 2017. CFD modeling of a industrial-scale steam methane reforming furnace. Chem. Eng. Sci. 171, 576–598.

Wang, Y., Gao, F., Doyle, F.J., 2009. Survey on iterative learning control, repetitive control, and run-to-run control. J. Process Control 19, 1589–1600.

Weckman, T., Shirazi, M., Elliott, S.D., Laasonen, K., 2018. Kinetic Monte Carlo study of the atomic layer deposition of zinc oxide. J. Phys. Chem. C 122, 27044–27058.

Young, D.F., Munson, B.R., Okiishi, T.H., Huebsch, W.W., 2010. A Brief Introduction to Fluid Mechanics. John Wiley & Sons.